A Phantom Study of Intracranial CSF Signal Loss Due to Pulsatile Motion

John A. Malko[1]
James C. Hoffman, Jr.[1]
Eric C. McClees[1, 2]
Patricia C. Davis[1]
Ira F. Braun[1]

MR imaging of the head often reveals localized areas of decreased signal intensity (flow voids) within the CSF. These flow voids are caused by turbulence within the CSF resulting from its pulsatile back-and-forth flow through the cerebral aqueduct and foramina. We describe a phantom that mimics the essential features of the CSF flow, and discuss its use in studying the dependence of the CSF flow void (CFV) on spin-echo (SE) and inversion-recovery pulse sequence parameters. The phantom had fluid-filled spaces to represent ventricles, and channels connecting these spaces to represent the aqueduct and foramina. A pump pushed the fluid in a pulsing manner through the phantom at various rates. The CFV was quantified by measuring signal loss relative to nonflowing fluid. The CFV did not appear to depend on repetition time or inversion time. The CFV was, however, strongly dependent on echo time (TE), and for single-echo SE sequences CFV became less severe as TE decreased. An even-echo rephasing effect was observed for multiecho sequences. Slice thickness and field of view also affected the appearance of the CFV, as did gating with respect to the pulsatile motion.

These results imply that TE, field of view, slice thickness, and gating must be considered when using the appearance or absence of the CFV in diagnosis.

MR imaging of the head and spine often reveals artifacts caused by the pulsatile back-and-forth movement of CSF [1–5]. These artifacts take the form of misplaced or "ghost" images of the CSF, signal loss throughout the entire CSF volume, or small regions of highly localized signal loss situated within the CSF (flow voids). A recent publication has described a phantom study of the first two of these CSF flow artifacts in the spine caused by pulsating laminar flow [5]. Such phantom studies are useful in that they allow an investigation of the effects of various parameters to be tested under fixed and controllable conditions. In this paper we describe the construction and use of a phantom to study the effect of various spin-echo (SE) and inversion-recovery (IR) pulse sequence parameters on the flow-void artifact seen in intracranial MR of the CSF spaces [1–3]. The localized intracranial CSF flow void (CFV) is thought to be caused by turbulent nonlaminar flow of the CSF as it pulsates between the CSF spaces through the small channels of the cerebral aqueduct and foramina [1]. The phantom was therefore constructed to exhibit nonlaminar turbulent flow by pushing the fluid in a pulsatile manner from one fluid-filled space to another through variously sized channels.

Received March 31, 1987; accepted after revision July 29, 1987.

[1] Department of Radiology, Emory University School of Medicine, 1364 Clifton Rd., N.E., Atlanta, GA 30322. Address reprint requests to J. A. Malko.

[2] Department of Radiology, Piedmont Hospital, Atlanta, GA 30309.

AJNR 9:83–89, January/February 1988
0195–6108/88/0901–0083
© American Society of Neuroradiology

Materials and Methods

Phantom Construction

The phantom was constructed from plastic tubes with regions to represent the volumes of the lateral, third, and fourth ventricles, and the cisterns. Holes were drilled in solid plastic to represent the cerebral aqueduct and foramina. The phantom was filled with a 0.5 mM copper sulfate and water solution to represent the CSF. The channels representing the foramina of Munro were 5.4 mm long and 2 mm in diameter; the channels for the cerebral aqueduct were 11.9 mm long and 1.6 mm in diameter; the foramina of Lushka and Magendie

were represented by holes 1.6 mm in diameter. These channels do not of course correspond to anatomic shapes, but were instead chosen to represent approximate average lengths and diameters [6–8]. Likewise, the spaces representing the ventricles were constructed to have anatomically relevant volumes [6, 8, 9]. A schematic of the spaces and channels is shown in Figure 1A. A second tube filled with stationary fluid was positioned below the flow phantom, and acted as a control for no-flow signal strength. This tube contained the same fluid as was in the flow phantom. The phantom was connected at one end by a long length of tubing to a fluid-containing reservoir and at the other end to a U-tube. Part of the fluid reservoir was enclosed by a rubber membrane; a motor-driven cam was positioned to beat on this membrane causing the fluid to be pushed in a periodic back-and-forth manner through the phantom at various displacement rates. The U-tube contained a mercury column whose height varied with the fluid displacement; the net fluid displacement per beat was measured by recording the highest and lowest mercury level. Figure 1B is a photograph of the flow phantom, pumping mechanism, and U-tube. To acquire data, the flow phantom was positioned inside the magnet, with the pumping mechanism and U-tube outside and connected to the phantom by tubing. An electrical circuit and resistive transducer (carbon rod immersed in the mercury column) gave an approximate linear conversion of the varying height of the mercury column into a time-varying voltage; this voltage was used as a signal for obtaining gated acquisitions. A representative strip-chart recording of this signal is shown in Figure 1C.

By adjusting the motor-driven cam, the net fluid displacement could be varied within the range 0–1.5 ml/beat. The beat rate varied between 40 and 80 beats/min.

Data Acquisition

The data were acquired on a Philips 1.5-T clinical imager. The phantom was positioned with its long axis along the direction of the main field. Data were acquired in the form of sagittal modulus images using a 256 × 256 acquisition matrix, a single 5- or 10-mm thick slice, and one measurement; the phase-encoding or warp direction was perpendicular to the long axis of the phantom. A standard clinical head coil 30 cm in diameter was used.

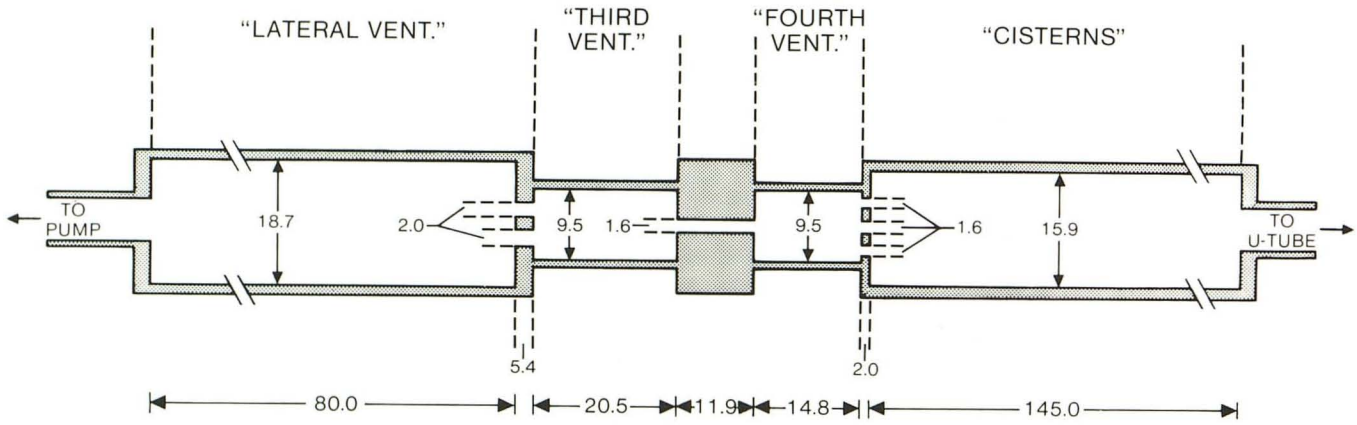

A

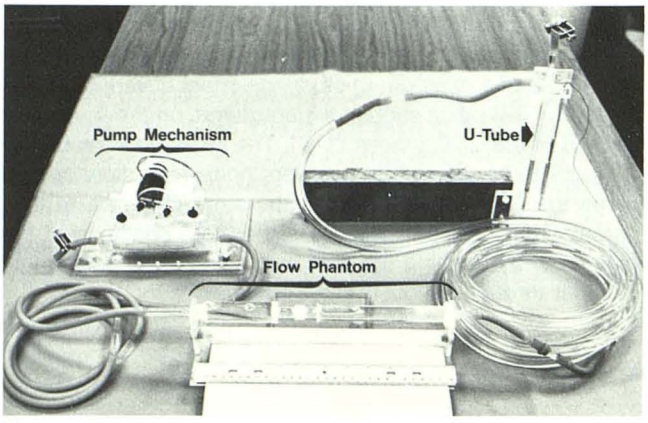

B

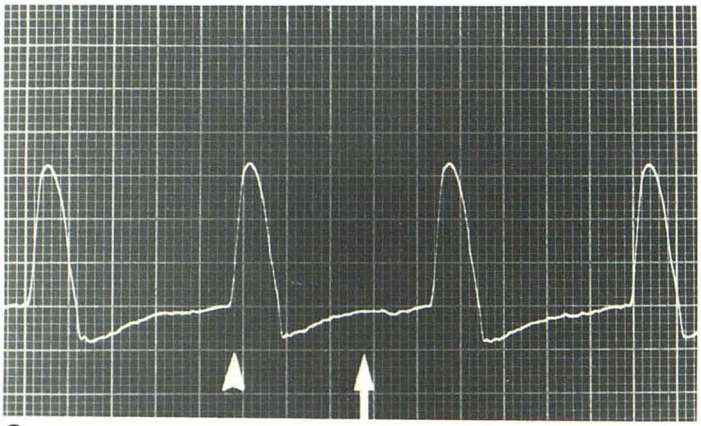

C

Fig. 1.—*A*, Schematic showing dimensions of spaces and channels in flow phantom. All dimensions in mm.

***B*, Photograph of pumping mechanism, flow-phantom, and U-tube. Tube containing stationary fluid is positioned below flow-phantom tube. Pump mechanism consists of motor, cam, and fluid reservoir. U-tube allows fluid displaced by pump to move a mercury column.**

***C*, Representative strip-chart recording of fluid displacement (vertical axis) versus time (horizontal axis). In this example, pump rate was approximately 65 beats/min with a total displacement of 0.1 ml/beat. *Arrowhead* and *arrow* indicate two different points at which gated data were obtained.**

With the phantom set pumping at various displacement rates, images were acquired for SE sequences with TR values of 250, 500, 1000, 1500, and 2000 msec, and TE values between 20 and 50 msec, and for IR sequences with TR = 1500 msec, TE = 30 msec, and inversion times (TI) of 200 and 1000 msec. Gated data were also acquired for various sequences.

Results

Figure 2A is an image of the phantom acquired with an SE sequence having TR/TE = 500/30 and no flow in the phantom. In this and all following images the space representing the lateral ventricular volume is on the top; the tube with stationary fluid is on the left. The fluid-filled spaces of the flow phantom are homogeneous in appearance and the small channels representing the cerebral aqueduct and ventricular foramina, though not perceptible on the photograph, can be made visible by changing the contrast level. The dark space in the tube with stationary fluid is caused by an air bubble.

Figures 2B–2D are images acquired with a constant displacement of approximately 0.3 ml/beat using an SE sequence with TR/TE = 500/21, 500/30, and 500/50 msec, respectively. In these images there are regions of marked signal loss (flow voids) in the flow phantom, and the cerebral aqueduct and foramina are not seen. The flow voids are more noticeable for the image acquired with the longest echo time. The nonuniformities in the tube with stationary fluid are caused by ghost images [5] from the flow phantom in the phase-encoding (horizontal) direction. In Figure 2E the displacement was reduced to approximately 0.1 ml/beat, and a TR/TE = 500/30 SE sequence was again used; the flow voids are not as pronounced as in Figure 2C, but are still present. To quantify changes of the flow void for different acquisition parameters, we measured the average pixel intensity in regions of interest (ROIs) centered on the fluid-filled spaces. Two such ROIs are shown in Figure 2F.

Figure 3 shows the quantified flow-void ratio for various values of TR/TE for SE sequences and TI for IR sequences. The flow-void ratio was defined as the ratio of the signal in ROI 1 (see Fig. 2F) for the flow and nonflow case. For these data the pump rate was set at approximately 65 beat/min and a displacement of 0.1 ml/beat. This displacement value is on the order of calculated in vivo pulsatile values [1]. We estimate the peak velocity in the 2-mm-diameter channels representing the foramina of Munro, for example, to be approximately 10 cm/sec, a value that is also comparable to estimated in vivo peak velocities [1]. The data in Figure 3

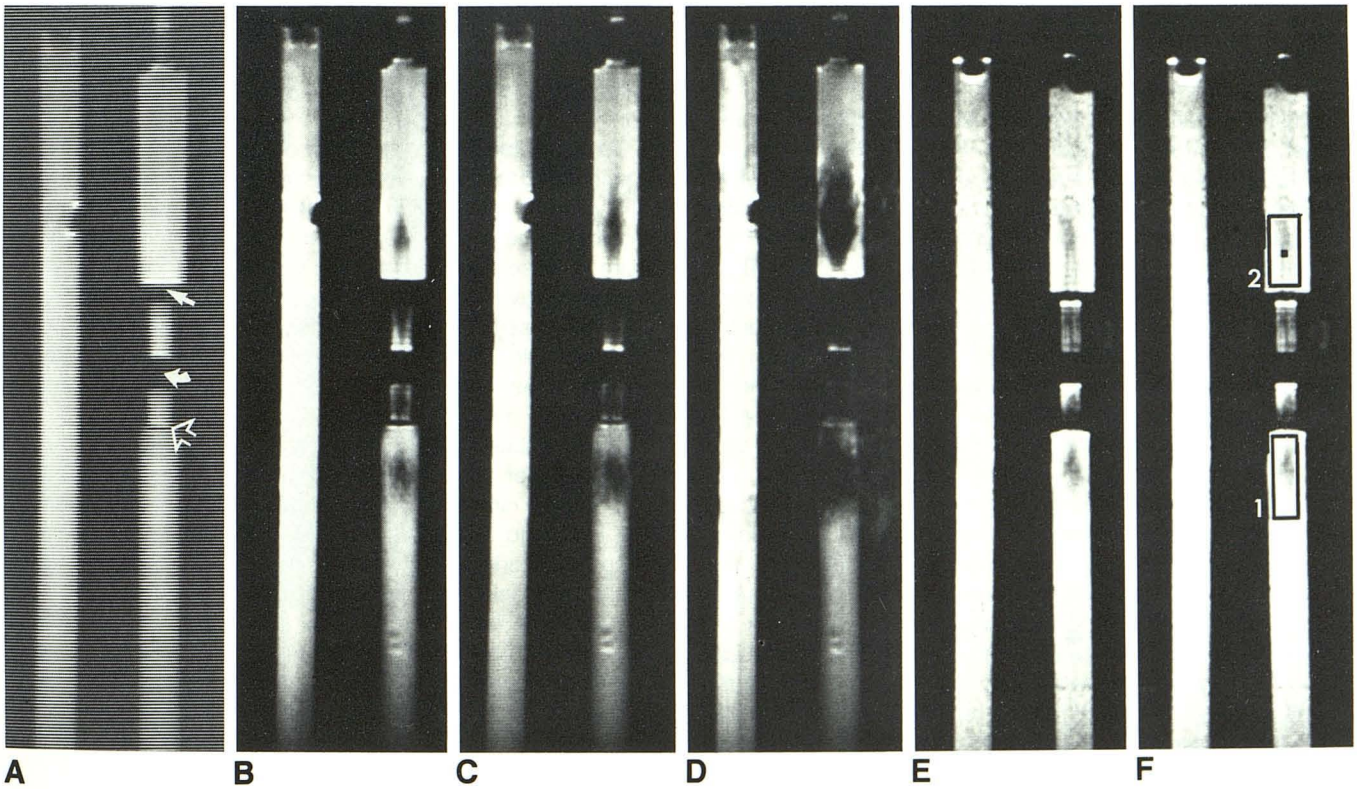

Fig. 2.—*A*, Image of phantom acquired with TR/TE = 500/30 msec SE sequence with no flow in the phantom. Regions of Foramina of Munro (*straight arrow*), aqueduct (*curved arrow*), and fourth ventricular foramina (*open arrow*) are shown. Dark space in tube with stationary fluid is caused by an air bubble.

***B–D*, Images of phantom with a displacement of 0.3 ml/beat flowing through phantom, acquired with SE sequence of TR/TE = 500/21 msec (*B*), TR/TE = 500/30 msec (*C*), and TR/TE = 500/50 msec (*D*).**

***E*, Image of phantom acquired with TR/TE = 500/30 SE sequence and a 0.1 ml/beat displacement flowing through phantom.**

***F*, Same conditions as 2E, but showing two ROIs used to quantify flow void.**

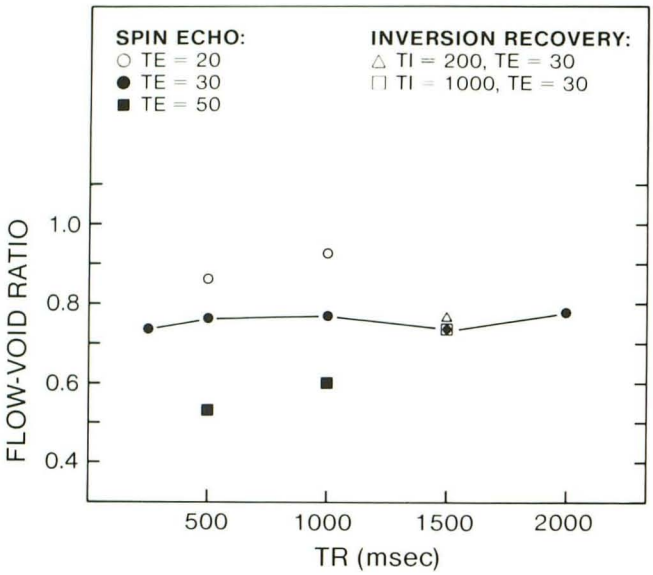

Fig. 3.—Quantified flow-void ratio for various TR, TE, and TI values. Solid lines connecting data points are visual aids.

show that the flow void is sensitive to TE and relatively insensitive to TR and TI. These results did not depend on which ROI was chosen to quantify the flow void or on the pump displacement.

Multiecho sequences exhibited an "even-echo rephasing" effect, as illustrated in Figures 4A–4D for an SE 500/30, 60, 90, 120 sequence. The even echoes in Figures 4B and 4D appear to have less severe flow voids than the odd echoes in Figures 4A and 4C. These results are quantified in Figure 4E for two different ROIs, as are the results for SE 500/20, 40, 60, 80 and 500/50, 100, 150, 200 sequences. The quantification was accomplished by again measuring the average signal intensity in ROIs centered on the flow void. Again, the qualitative features of the multiecho data did not depend on ROI or pump specifics; in all cases tried, the second echo showed less flow void than the first echo; the third more than the second.

Figure 5 shows the results of gating a TE = 30 msec SE acquisition using the cyclic time-varying signal supplied by the phantom; a strip-chart recording of this signal is shown in Figure 1C. For these data the pump rate was 65 beats/min with a displacement of 0.1 ml/beat. Figure 5A shows the image obtained by gating on the up slope or maximum velocity part of the signal (*arrowhead*, Fig. 1C); Figure 5B shows the image obtained by gating on a relatively flat or minimum velocity part of the signal (*arrow*, Fig. 1C). These results show that the severity of the flow void can be reduced by proper gating.

A number of images were acquired with a reduced slice thickness or a reduced field of view. Figures 6A and 6B compare the appearance of the flow void as the slice thickness is changed from 10 mm to 5 mm for a 500/30 SE sequence. Figures 6C and 6D show the result of changing the field of view from 300 mm to 200 mm. These images demonstrate that the flow void is more apparent for the smaller slice thickness and for the smaller field of view.

One advantage of a phantom study is to allow tests that are clinically difficult to perform. To this end, the pumping mechanism was removed and a steady flow was set up through the phantom to mimic the effect of the bulk CSF flow, which is thought to be approximately 0.4 ml/min [10]. With a flow of approximately 1 ml/min moving through the phantom no flow-void effects could be seen.

Discussion

The phantom data obtained here show that for the SE and IR pulse sequences used the flow void is more strongly dependent on TE than on TR or TI, and that the flow void decreases as TE decreases for a single-echo sequence. For multiecho sequences an even-echo rephasing effect was observed. Field of view and slice thickness were both found to affect the size of the flow void. These results were not found to depend on the region of the phantom used to measure the flow void or on the specifics of the pump displacement. The only dependence on pump rate was the trivial one sometimes observed when pump rate and TR were even multiples of each other, resulting in pseudogated images. Since the various regions of the phantom in which the flow void was visualized were adjacent to channels having different sizes and configurations, we conclude that the results are not specific to the details of the phantom construction.

To understand the applicability of these results to other MR imagers and to the in vivo situation requires an understanding of the origin of the flow void. It is well known that a spin moving in the environment of the imaging gradients will acquire a phase change relative to nonmoving spins [11, 12]. In turbulent flow the spins in any one image voxel can have different phases as a result of their having different velocities; the flow void is thought to be due to a cancellation of the signals of the spins, which are out of phase with one another within each image voxel [13].

The absolute severity of the flow void therefore depends on the size of the velocity spread within an image voxel, and this velocity spread depends on the net fluid displacement per beat and the minutiae of details concerning the size, shape, and orientation of the spaces and channels through which this displaced fluid is forced and the resulting turbulence pattern thereby set up. Thus, for example, in Figure 2C, the flow voids in the various phantom spaces are all seen to be of different severity.

The results for the dependence of the flow void on pulse sequence parameters can be understood as follows: for an SE or IR sequence the spins are tipped into the transverse plane by the 90° pulse, at which time they begin to precess in the presence of the imaging gradients. The phantom data were acquired with the warp or phase-encoding gradients perpendicular to the long axis of the phantom, and hence the readout gradient along the direction of average flow. This orientation approximates the usual clinical situation in which

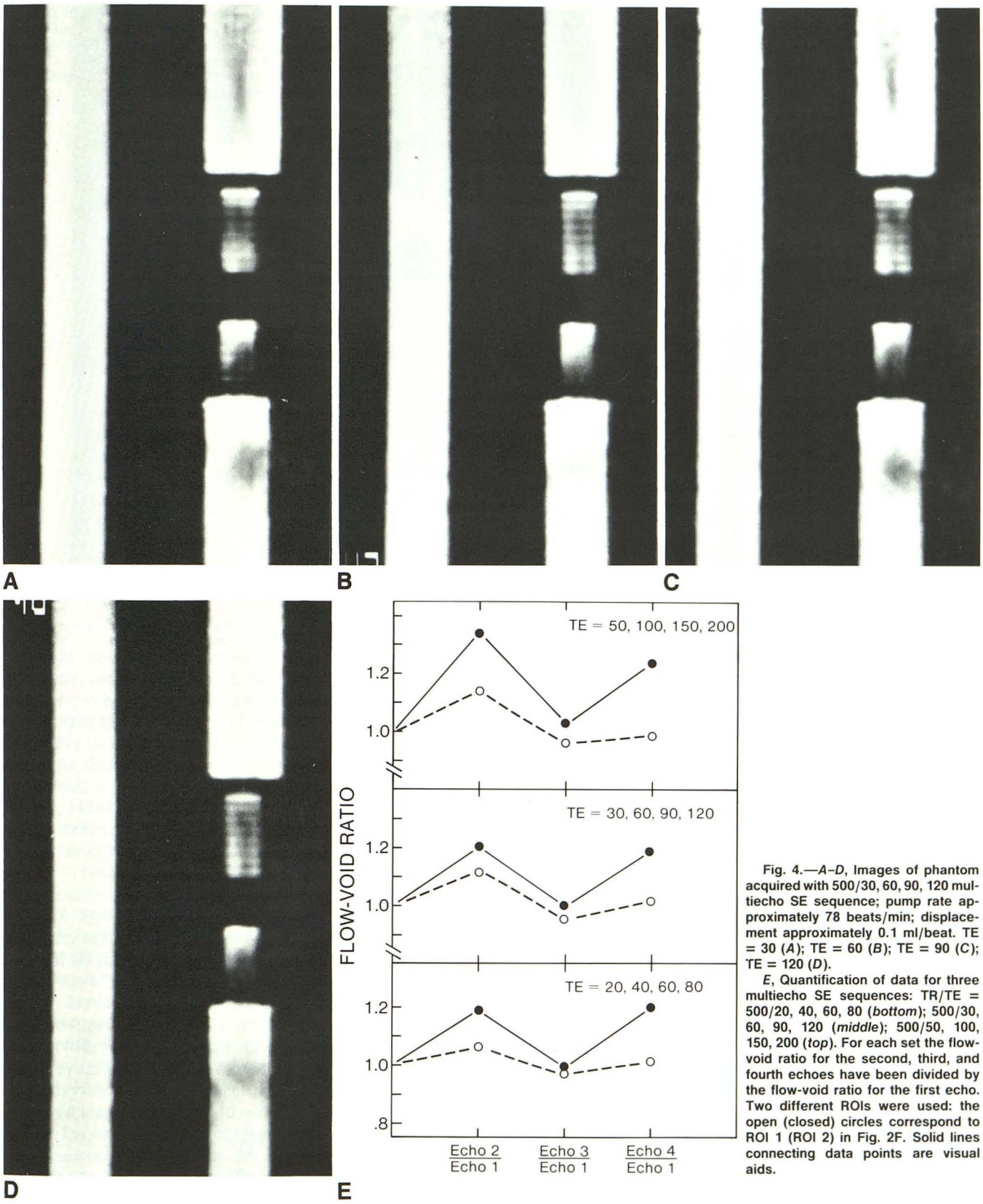

Fig. 4.—*A–D*, Images of phantom acquired with 500/30, 60, 90, 120 multiecho SE sequence; pump rate approximately 78 beats/min; displacement approximately 0.1 ml/beat. TE = 30 (*A*); TE = 60 (*B*); TE = 90 (*C*); TE = 120 (*D*).

E, Quantification of data for three multiecho SE sequences: TR/TE = 500/20, 40, 60, 80 (*bottom*); 500/30, 60, 90, 120 (*middle*); 500/50, 100, 150, 200 (*top*). For each set the flow-void ratio for the second, third, and fourth echoes have been divided by the flow-void ratio for the first echo. Two different ROIs were used: the open (closed) circles correspond to ROI 1 (ROI 2) in Fig. 2F. Solid lines connecting data points are visual aids.

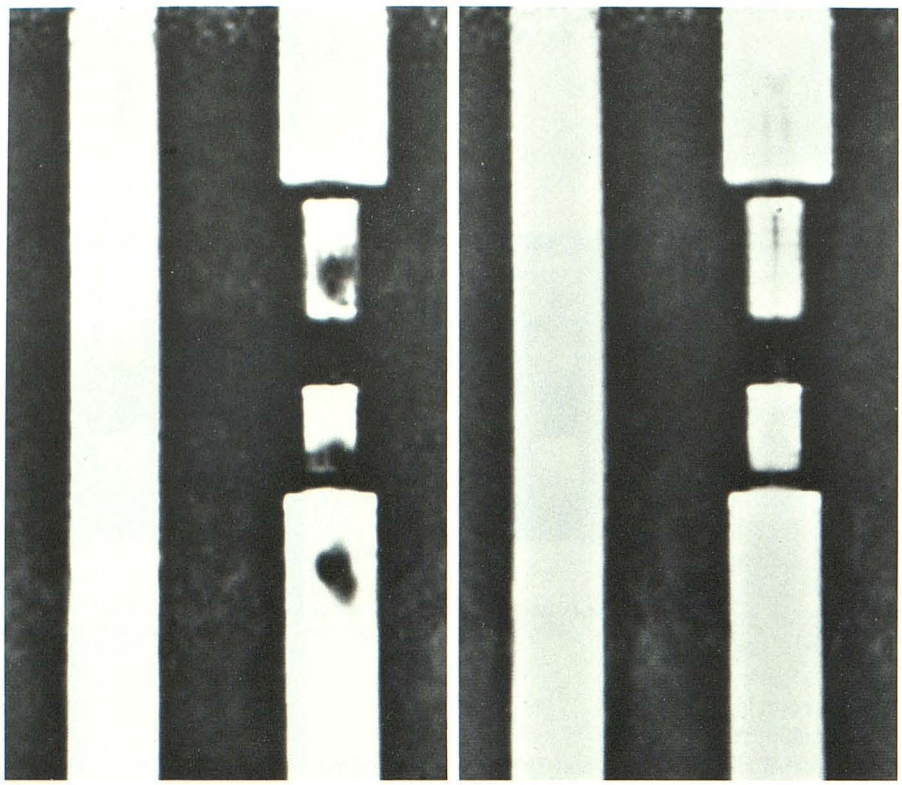

Fig. 5.—Results of gating a TE = 30 msec SE acquisition at two different points in flow cycle.
***A*, Image obtained by gating during maximum flow (*arrowhead*, Fig. 1C).**
***B*, Image obtained by gating during minimum flow (*arrow*, Fig. 1C).**

sagittal images are obtained with the phase encoding in the ventrodorsal direction and hence the CSF flow in an approximate craniocaudal direction. An analysis of standard SE and IR pulse sequences for flow along the readout direction shows that besides a dependence on echo time (which is quadratic for constant velocity spins), the flow-dependent phase depends on the details of when the readout gradient is turned on and off [13, 14]. If this readout gradient timing is independent of TR or TI, then the velocity-dependent phase will also be independent of TR or TI, as will the resulting flow void.

Since the turbulent flow results in spins with velocity components in all directions, it follows that all the imaging gradients can contribute to dephasing. Any parameter that affects the strength of the imaging gradients can therefore affect the amount of dephasing, and hence the flow void. Slice thickness, image field of view (FOV), and image resolution (R) all depend on gradient strength. For 2DFT imaging the ratio R/FOV is proportional to the maximum image gradient. Hence, decreasing the FOV or increasing R will increase gradient strength. Likewise, decreasing the slice thickness will also increase gradient strength.

Our data indeed show the flow void to increase for decreasing FOV (Figs. 6C and 6D), and for decreasing slice thickness (Figs. 6A and 6B). The change in slice thickness from 3.5 mm to 2.5 mm causes a 40% increase in gradient slice selection strength and a minimal partial volume effect. We note that a recent publication has also reported the clinical observation of an increase in the flow void for decreasing slice thickness [15]. However, decreasing either the FOV or slice thickness also decreases the size of the image voxel over which the dephased spins are summed, and this can in fact reduce the severity of the flow void. We conclude that the dependence of FOV and slice thickness may not be as simple as that shown by our data. Our data also demonstrate an even-echo rephasing effect. The mechanism for even-echo rephasing has been described previously [13, 16] and is due to the action of the imaging gradients on constant velocity spins. Hence, the magnitude of the rephasing is dependent on the amount of fluid with constant velocity components, and therefore dependent on the experimental arrangement.

The results from the gated acquisition demonstrate that gating can affect strongly the severity of the flow void. (An earlier study demonstrating the effects of cardiac gating on transaxial images of the cerebral aqueduct can be found in [17].) The curve in Figure 1C is proportional to the height of the displaced fluid as a function of time; therefore, at any time, the flow and velocity in a channel are related to the slope of this curve. It is not surprising that the flow void observed when gating on the flat portion of this curve (smallest flow) (Fig. 5B) is much less than that observed when gating on the steepest portion of the curve (largest flow) (Fig. 5A). How these results transfer to the in vivo case will depend in detail on the shape of the corresponding curve for the various CSF spaces, which will in turn depend on the different expansion properties of these spaces. We note that with our pumping arrangement the same displacement per beat is obtained for all regions of the phantom, while for the in vivo case the various CSF spaces could have different expansion properties.

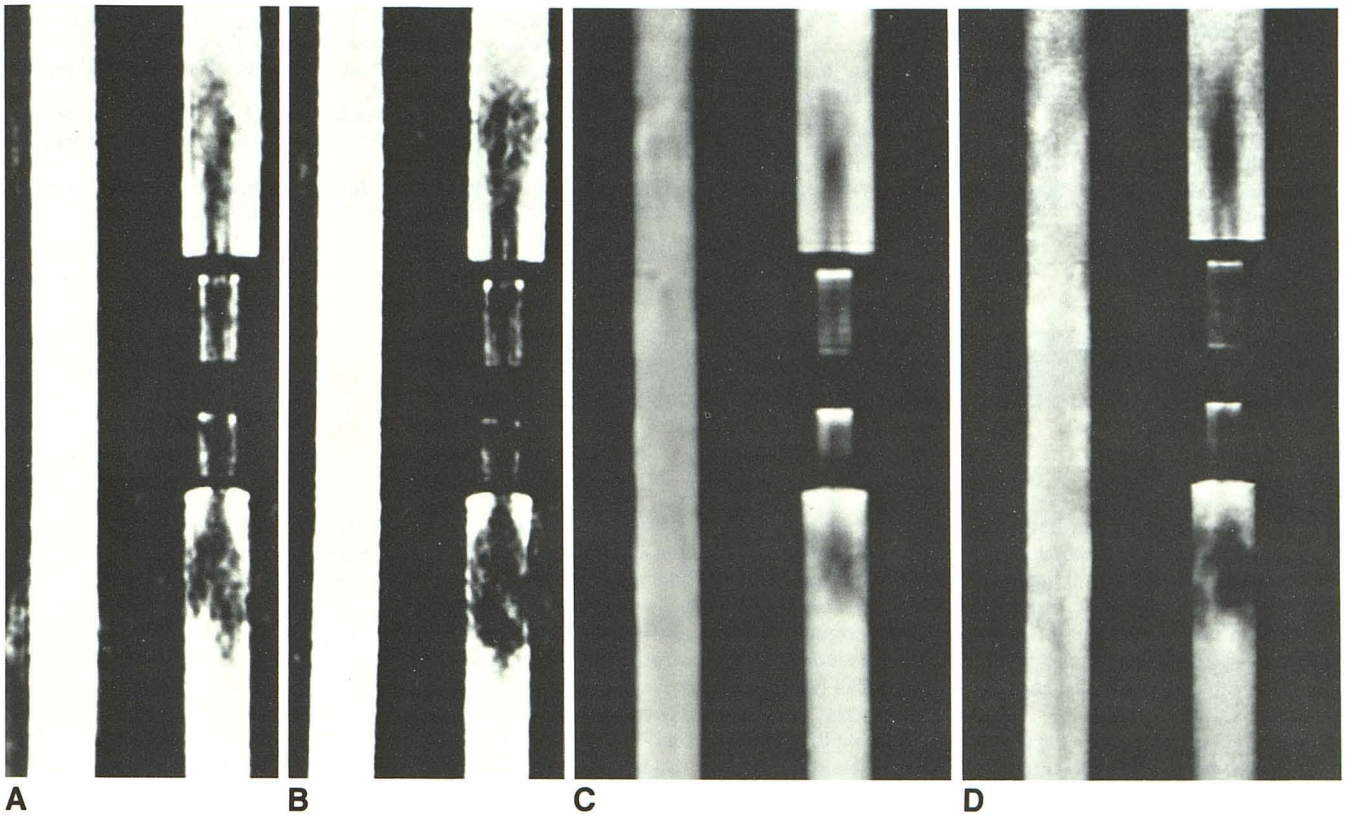

Fig. 6.—*A*, *B*, Effect of changing slice thickness from 3.5 mm (*A*) to 2.5 mm (*B*) for a 500/30 SE sequence. *C*, *D*, Effect of changing the field of view from 300 mm (*C*) to 200 mm (*D*) for a 500/30 SE sequence.

The severity of the flow void depends on the amount of dephasing between the spins in the image voxel, and this dephasing depends on the strength of the gradients and the amount of time for which they are experienced. Multislice imaging uses more gradients and hence can affect the severity of the flow void. However, the dependences on TR, TE, TI, and so on should still remain.

To summarize, we conclude that while the magnitudes of the flow voids seen with our phantom are specific to the details of the phantom design, the general results concerning the relationship of the flow void to the imaging parameters are applicable to other MR imagers. Our results imply that echo time is the most important factor affecting the appearance of the flow void, and that field of view, slice thickness, and gating can also affect the appearance of the flow void. All of these must therefore be considered when using the presence or absence of the flow void for clinical diagnosis.

REFERENCES

1. Sherman JL, Citrin CM. Magnetic resonance demonstration of normal CSF flow. *AJNR* **1986**;7:3–6
2. Sherman JL, Citrin CM, Bowen BJ, Gangarosa RE. MR demonstration of altered cerebrospinal fluid flow by obstructive lesions. *AJNR* **1986**;7:571–579
3. Burt TB. MR of CSF flow phenomenon mimicking basilar artery aneurysm. *AJNR* **1987**;8:55–58
4. Enzmann DR, Rubin JB. Imaging of spinal CSF pulsation by 2DFT MR: significance during clinical imaging. *AJNR* **1987**;8:297–306
5. Rubin JB, Enzmann DR. Harmonic modulation of proton MR precessional phase by pulsatile motion: origin of spinal CSF flow phenomena. *AJNR* **1987**;8:307–318
6. Bentson JR, Alberti J. The fourth ventricle. In: Newton TH, Potts DG, eds. *Radiology of the skull and brain—ventricles and cisterns*. St. Louis: Mosby, **1978**:3303–3362
7. Schecter MM. The aqueduct. In: Newton TH, Potts DG, eds. *Radiology of the skull and brain—ventricles and cisterns*. St. Louis: Mosby, **1978**:3363–3397
8. Rosenbaum AE, Hawkins RL, Newton TH. The third ventricle. In: Newton TH, Potts DG, eds. *Radiology of the skull and brain—ventricles and cisterns*. St. Louis: Mosby, **1978**:3398–3488
9. Deck MDF. The lateral ventricles. In: Newton TH, Potts DG, eds. *Radiology of the skull and brain—ventricles and cisterns*. St. Louis: Mosby, **1978**:3489–3587
10. Cutler RW, Page L, Galicich J, Watters GV. Formation and absorption of cerebrospinal fluid in man. *Brain* **1968**;91:707–719
11. Hahn EL. Detection of sea-water motion by nuclear precession. *J Geophys Res* **1960**;65:776–777
12. Moran PR. A flow velocity zeugmatographic interlace for NMR imaging in humans. *Mag Reson Imag* **1982**;1:197–203
13. Von Schulthess GK, Higgins CB. Blood flow imaging with MR: spin-phase phenomena. *Radiology* **1985**;157:687–695
14. Van Dijk P. Direct cardiac NMR imaging of heart wall and blood flow velocity. *J Comput Assist Tomogr* **1984**;8:429–436
15. Enzmann DR, Rubin JB, DeLaPaz R, Wright A. Cerebrospinal fluid pulsation: benefits and pitfalls in MR imaging. *Radiology* **1986**;161:773–778
16. Waluch V, Bradley WG. NMR even echo rephasing in slow laminar flow. *J Comput Assist Tomogr* **1984**;8:594–598
17. Bergstrand G, Bergstrom M, Nordell B, et al. Cardiac gated MR imaging of cerebrospinal fluid flow. *J Comput Assist Tomogr* **1985**;9:1003–1006